Wall pressure fluctuations over a serrated trailing edge at different angles of attack

Lima Pereira, L.T.; Avallone, F.; Ragni, D.

DOI
10.2514/6.2021-2179

Publication date
2021

Document Version
Final published version

Published in
AIAA AVIATION 2021 FORUM

AIAA AVIATION Forum
August 2-6, 2021, VIRTUAL EVENT
AIAA AVIATION 2021 FORUM

10.2514/6.2021-2179

Wall-pressure fluctuations over a serrated trailing edge at different angles of attack

Lourenço T. Lima Pereira*, Francesco Avallone†, and Daniele Ragni‡
Delft University of Technology, Delft, The Netherlands, 2628 CD

The unsteady surface pressure fluctuations over trailing-edge serrations retrofitted to the benchmark NACA 63_3-018 profile are experimentally measured. Miniaturized unsteady pressure transducers installed on the serration surface are used to describe the temporal and spatial distribution of the wall-pressure fluctuations over the trailing-edge add-on. The measured spectra, convection velocity, and correlation lengths of the surface pressure fluctuations are presented for the most upstream sensor and compared against the data at different locations along the serration surface. Different angles of attack are tested in a Reynolds number of 2×10^6 (based on the airfoil chord) in order to describe the properties of the wall-pressure fluctuations at a range of representative conditions for wind turbine applications. The study details the characteristics of the wall-pressure fluctuations on the serration surface. In particular, the distribution of the wall-pressure fluctuations with and without aerodynamic loading caused by the variation of the airfoil angle of attack is shown, highlighting the impact of the vortex pairs formed around the edges of the serrations under loading on the wall-pressure fluctuations. The experimental results focus on the modifications of the wall-pressure fluctuations over the serration surface. Results show that, at small angles of attack, the amplitude of the wall-pressure fluctuations is higher at the serration root for low frequencies and at the serration tip for high frequencies. As the angle of attack increases, the aerodynamic loading over the serrations causes an increase in the wall-pressure fluctuations around the edges of the serrations. This increase depends on the incoming fluctuations from the boundary layer and is related to the degradation of serration acoustic performance at angle. Furthermore, the experimental results corroborate to the benchmark activities for trailing-edge serration noise carried out in collaboration with DTU and DLR, providing information about the pressure fluctuations measured near the edges of the serration.

I. Nomenclature

x, y, z	=	Streamwise , spanwise and wall-normal directions
$2h$	=	Serration height
c	=	Airfoil chord
C_p	=	Pressure coefficient
f	=	Frequency
H	=	Boundary-layer shape factor (δ^*/θ)
l_x	=	Streamwise correlation length
l_z	=	Spanwise correlation length
Re	=	Reynolds number based on the airfoil chord
Re_δ	=	Reynolds number based on δ_{99} and U_e
U_c	=	Convection velocity
U_e	=	Edge velocity
U_∞	=	free stream velocity
u_τ	=	Friction velocity
α	=	Airfoil angle of attack
β_θ	=	Pressure gradient parameter

*PhD candidate, Delft University of Technology, L.T.LimaPereira@tudelft.nl, and AIAA Member.
†Assistant professor, Delft University of Technology, and AIAA Member.
‡Associate professor, Delft University of Technology, and AIAA Member.

γ = Coherence between two sensors
δ_{99} = Boundary layer height at $99\%U_e$
δ^* = Boundary layer displacement thickness
Δ_* = δ_{99}/δ^*
Δx = Distance between two sensors in the streamwise direction
λ = Serration wavelength
θ = Boundary layer momentum thickness
ψ = Phase of the cross-correlation between two sensors
ϕ_{pp} = Power spectral density of the wall-pressure fluctuations
ω = Radial frequency
Π = Wake parameter

II. Introduction

Wind turbine noise is a growing concern with the increasing diameter of modern wind turbine blades [1]. It has been shown that the scattering of the acoustic waves at the blade trailing edge is the predominant source of noise [2]. With this in mind, many manufactures have included trailing-edge serration add-ons in their portfolio as a way to reduce wind turbine noise [3]. The add-ons reduce the scattering efficiency by creating an angle between the convecting turbulent structures and the trailing edge.

However, although serrations are widely used, their noise prediction is still an ongoing subject of research [4–8], since large deviations between theoretical predictions and measurements are often reported [9, 10]. Consequently, the design of wind turbine serrations relies solely on dedicated experiments or advanced numerical simulations, hampering the fast assessment provided by analytical methods. Experimental works [9, 11] and numerical ones [12–14] pointed out important modifications of the flow along the trailing-edge serrations. The observed deviations from the scattering predictions are, therefore, attributed to the inaccurate representation of the flow near the serrations, generally idealized as the pure advection of the fluctuations from the turbulent boundary layer developed upstream following Taylor's frozen turbulence assumption [15]. These deviations are particularly higher when the serrations are put at an angle with respect to the flow direction and the same produces aerodynamic loading. It is shown that the effect of the aerodynamic loading disrupts the noise reduction achieved with serrations [10, 16, 17]. The former studies have linked this increase in the noise emitted with the formation of a pair of counter-rotating vortices on the serration edges when aerodynamic loading is created.

Therefore, assessing the flow near the serrated trailing edges is necessary to properly describe noise in the far field. Experimentally, this is a very challenging task, given the small thickness of the serrations and the required spatial and temporal distribution of the measurements. 3D-PIV measurements [11, 13, 18] have helped to understand the flow behavior near the serrations. Nevertheless, this technique is limited to lower speeds yielding a lack of flow data at representative Reynolds numbers for wind turbine applications. Developments of MicroElectroMechanical Systems (MEMS) have enhanced the possibilities for aeroacoustic measurements. Smaller and affordable sensors can be installed near the edges of the model with ease. This enables measurements on the surface of trailing-edge serrations, as demonstrated in Sanders et al. [19], to cover the necessary spatial resolution and without the limitations for the flow speed and frequency range from PIV techniques.

Lead by the Technical University of Denmark (DTU) and with contributions from the German Aerospace Center (DLR), and the Delft University of Technology (TUD), a benchmark activity is proposed for providing experimental data on an airfoil equipped with trailing-edge serrations (BANC workshop). The benchmark consists of acoustic and steady aerodynamic measurements of a 2D NACA 63_3-018 airfoil section equipped with sawtooth serrations in different facilities. This work describes a complementary activity performed at the Delft University of Technology (TUD) to study the unsteady characteristics of the wall pressure on the surface of the benchmark sawtooth serrations. Measurements conducted with a wall-mounted printed circuit board (PCB) containing 22 microphone sensors on top of the serration add-on are carried out and the distribution of the wall-pressure fluctuations on the trailing edge serration under different flow conditions is presented. Focus is given on the modifications of the wall-pressure fluctuations over the serration and on the effect of aerodynamic loading over the serrations caused by the variation of the angle of attack.

III. Experimental setup

The experiments are conducted in the Low Turbulence wind Tunnel (LTT) at the Delft University of Technology (TUD). The model has a chord (c) of 0.9 m, 1.25 m span, and was developed for the future Benchmark problems for Airframe Noise Computation exercise on trailing-edge serrations (BANC). The exercise proposes tests that cover a wide range of operating conditions for wind turbine applications. Therefore, the model is tested at speeds of 17, 34, and 51 m/s, corresponding to Reynolds numbers of 1, 2, and 3 million, and at angles of attack (α) from 0 to 10^o. For the benchmark activities, lower Reynolds numbers are achieved testing a smaller model at the A-tunnel in TUD [20], and higher ones at the Poul la Cour facility in DTU.

The test section of the LTT wind tunnel is acoustically treated using foam covered with Kevlar walls. Fig. 1(a) shows the model installed inside the section. The model is tripped at 5%c at the pressure side with 0.8 mm zig-zag trip and at the suction side with 0.4 mm zig-zag trip.

A sawtooth serration of $2h$ = 90 mm, λ = 45 mm, thickness of 1 mm, and 2 mm radius at the junctions is manufactured in steel. The add-on is attached to one side of the model and a bend angle of 3.2° (equivalent to the trailing-edge angle) is given to the piece so the serration is aligned with the airfoil chord.

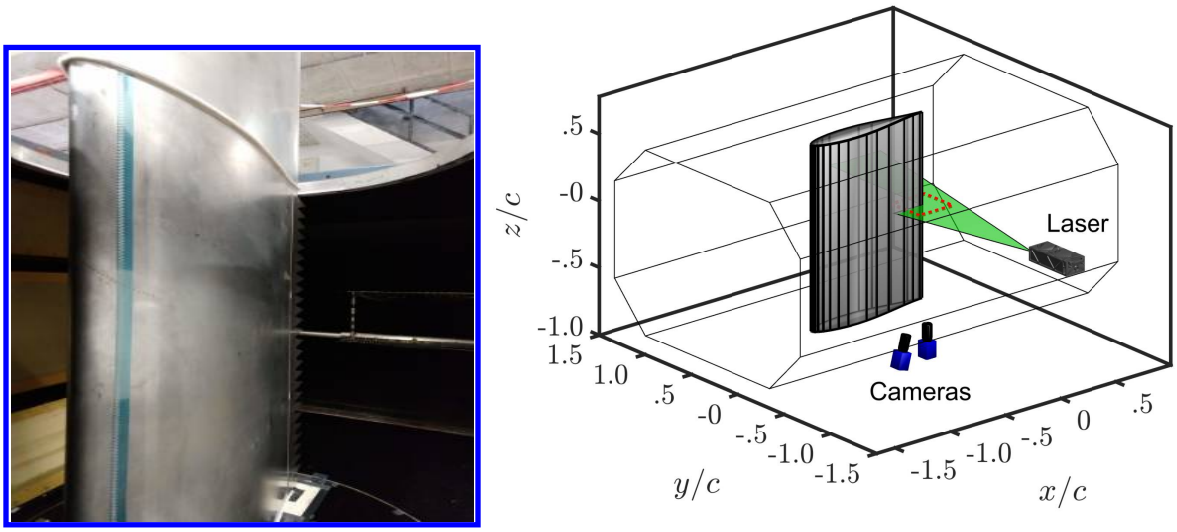

(a) (b)

Fig. 1 BANC NACA 63_3-018 2D wing model mounted inside the LTT wind tunnel with Kevlar test section (a) and illustration of the model, test section and PIV setup (b).

A. Surface pressure distribution and trailing edge boundary layer measurements

The pressure distribution over the airfoil model is monitored with 50 surface pressure taps at each side of the model. No pressure taps are installed on the serration surface, and the lift on that surface can only be indirectly observed by its influence on the upstream taps.

To capture the flow field near the trailing edge, a stereo PIV technique is used [21]. Two Imager sCMOS cameras (double shutter with 120 ns interframe time, 16 bits, 5MP) are placed outside the test section, 0.8 m apart from the illumination plane, one aligned with the trailing-edge line, and the second one forming an arc 20° upstream of the first. Imaging access is given by placing a Plexiglas wall on the turn-table. A Quantel Evergreen double pulsed laser (200 mJ, 15 Hz) is fixed on one of the side walls and a laser sheet is created normal to the model plane. Measurements are performed for the baseline at α = 0°, and 4° in order to extract the boundary-layer profiles at the trailing edge. Figure 1(b) shows an illustration of the PIV setup and Table 1 summarizes the properties of the PIV technique employed.

Table 1 Description of the Stereo PIV set-up for the measurement campaign.

Parameter	Value	
Digital image resolution	18	px/mm
Numerical aperture	$f/11$	
Field of view ($x \times y$)	150×100	mm
Number of images recorded	1,000	
Maximum particle displacement	15	px
Vector resolution	0.3	mm
Uncertainty in instantaneous velocity	0.7	$\%U_\infty$

B. Unsteady wall-pressure sensors

22 Sonion P8AC03 unsteady pressure sensors are placed over the sawtooth serrations as shown in Fig. 2. The sensors capture the pressure fluctuations, then used for building spectral and correlation statistics along the serration. A 0.4 mm thick printed circuit board (PCB) is mounted on top of the trailing-edge insert. The insert is manufacture in order to house the sensors inside, avoiding interference from both sides of the model. The multiple sensors and selected coordinates allow for the following analysis:

- Wall-pressure spectrum around the serration edges, using the sensors along the edge;
- Streamwise correlation and convective velocity, from the streamwise oriented central row;
- Spanwise correlation length, from the 4 spanwise rows along the serration;
- Distribution of the wall-pressure fluctuations over the serrations, from the data of the sensors interpolated over the serration surface (symmetry is assumed along the $z = 0$ axis).

The calibration of the sensors is performed with a Linear-X M51 microphone measuring an acoustic field close to the serrations. The Linear-X microphone is previously calibrated with a G.R.A.S. 42AA pistonphone. Acquisition is performed with NI cDAQ-9234 boards attached to a synchronous NI cDAQ-9189 chassis. The data is sampled at a rate of 51,200 samples per second for 20 seconds.

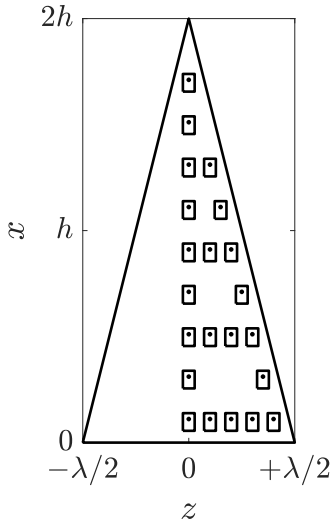

Fig. 2 Location of the unsteady pressure sensors at the trailing-edge serration.

IV. Results and discussions

A. Mean flow conditions

The pressure distribution over the model is compared to data obtained from X-Foil in Fig. 3. As observed, for angles from 0 to 8°, the pressure distribution compares well with the predictions. The presence of the sawtooth serration does not influence the flow along the airfoil indicating the correct alignment with the airfoil symmetry line. It is therefore supposed that the turbulent boundary layer develops similarly for both the baseline and serrated case, as also observed in Avallone et al. [14]. This former confirmation is relevant for the analyses as results are often non-dimensionalized with respect to the properties of the boundary layer predicted without the presence of the serration.

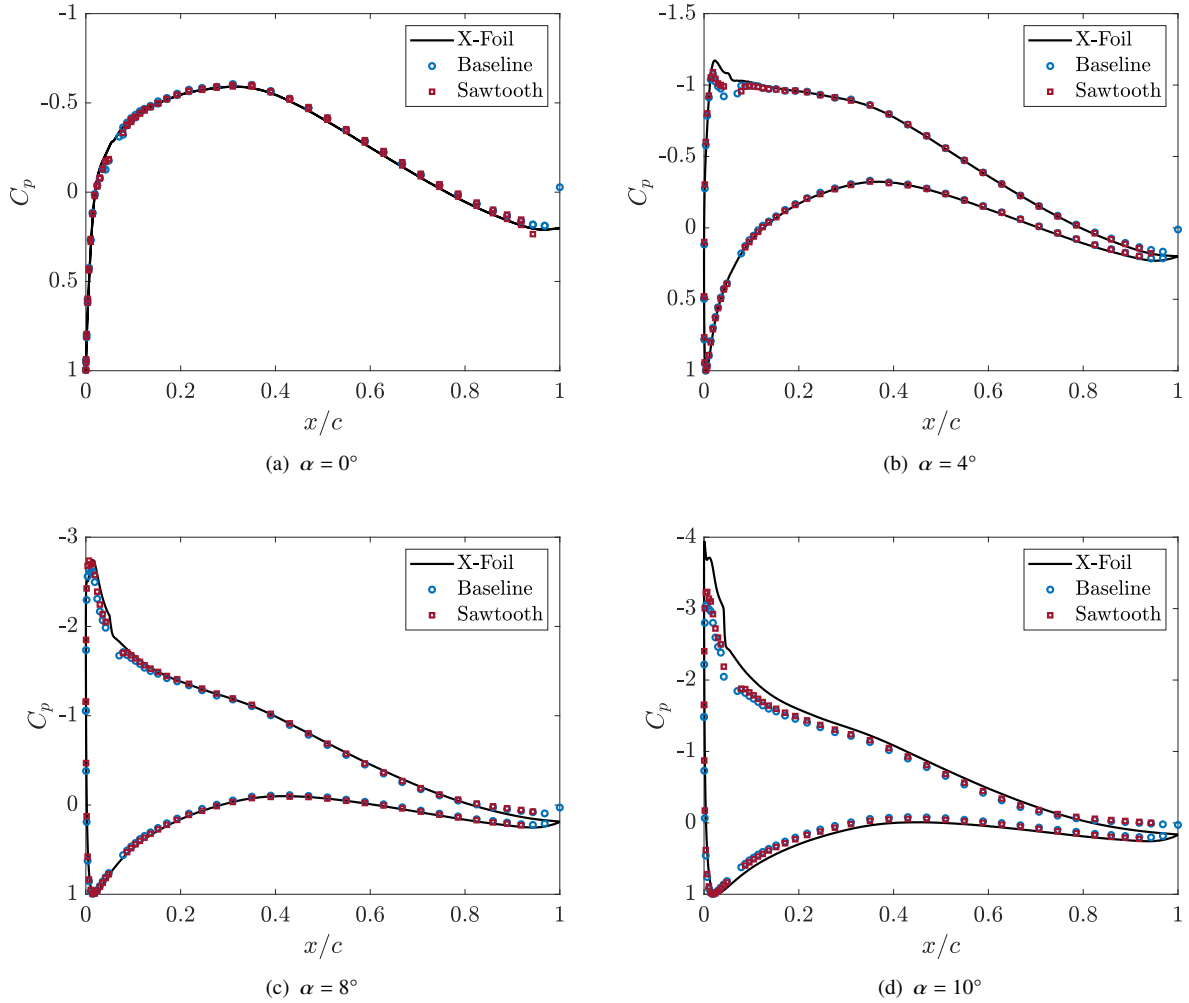

Fig. 3 Pressure distribution at different angles of attack compared against X-Foil predictions (Re = 2, 000, 000).

Fig. 4 shows the flow field captured near the trailing edge from the PIV measurements. The flow is measured for 0° and 4°. The boundary-layer profiles are extracted at 98%c (indicated with the wall-normal lines in Fig. 4) to avoid possible errors caused by the reflections at the exact trailing-edge region. Fig. 5 shows the 3 boundary layer profiles extracted ($\alpha = 0°$, $\alpha = 4°$ suction and pressure side) in wall units. Using Clauser's approach [22] the friction velocity u_τ can be estimated. The wake profile [23], represented by the dashed colored lines, improves the predictions for the different pressure gradient boundary layers, and is known to impact the wall-pressure fluctuations in adverse pressure gradients boundary layers [24]. Table 2 lists the parameters of the boundary layers extracted from the PIV technique and compares them with the predictions from X-Foil. The comparable results obtained with X-Foil indicate that the

predictions from the software are reasonably in agreement with the data and can be used for the non-dimensionalization of the variables at other conditions, where the boundary layer integral parameters are not collected (e.g. other angles of attack).

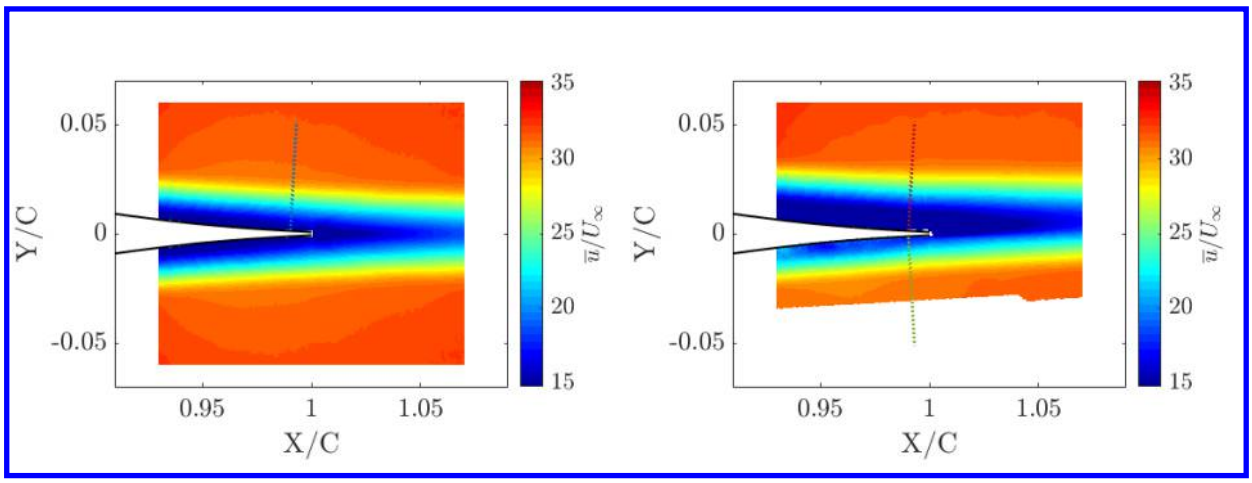

(a) $\alpha = 0°$ (b) $\alpha = 4°$

Fig. 4 Flow field near the trailing edge for the baseline case at $\alpha = 0°$ (a), and $\alpha = 4°$ (Re = 2, 000, 000). Wall normal lines denotes the region where the boundary-layer profile was extracted.

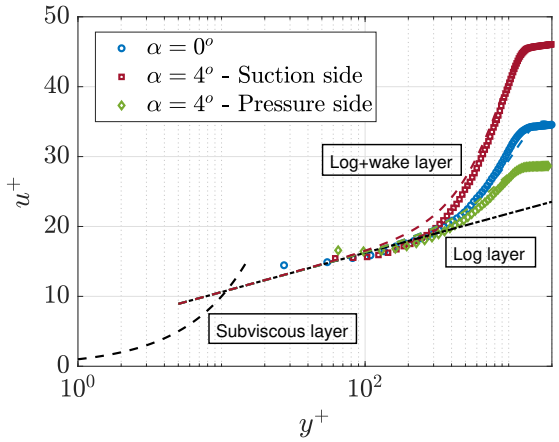

Fig. 5 Boundary-layer profile near the trailing edge for the baseline case at $\alpha = 0°$ (a), and $\alpha = 4°$ (Re = 2, 000, 000).Linear, logarithmic and logarithmic + wake laws are plotted.

B. Wall-pressure fluctuations at the serration root

In this section, the properties of the wall-pressure fluctuations at the serration root are shown. The data at the serration root are taken as reference incoming flow conditions. Further sections study the deviations on the wall-pressure fluctuations with respect to the root conditions.

Fig. 6 shows the variation of the pressure spectrum with the angle of attack captured at the root of the serration. The blue shades represent the spectrum measured at the pressure side (PS) and the red ones at the suction side (SS). Fig. 6(a) shows the captured spectra versus dimensional frequency while Fig. 6(b) shows the data scaled according to the predicted boundary layer properties. As the angle of attack increases, the amplitude at the suction side progressively increases at the lower frequencies while decreasing at the higher frequencies. The opposite trend is observed at the

Table 2 Boundary-layer parameters captured with the PIV measurements at Re = 2, 000, 000. Values in parenthesis indicate predictions from the X-Foil code.

Parameters	$\alpha = 0°$	$\alpha = 4°$ (SS)	$\alpha = 4°$ (PS)
U_e [m/s]	31.5	31.5	31
U_e/U_∞	0.89	0.89	0.88
δ_{99} [mm]	27	30	17
δ^* [mm]	6.1 ((5.3)	9.0 (8.4)	3.4 (3.6)
θ [mm]	3.9 (3.4)	4.8 (4.7)	2.8 (2.6)
Re_δ	56,700	63,200	35,100
H	1.59	1.87	1.29
Δ_*	4.4	3.3	5.0
u_τ [m/s]	0.91 (0.94)	0.69 (0.78)	1.08 (1.08)
Π	2.45	4.79	1.41
β_θ	-1.18 (FPG)	7.28 (APG)	-0.24 (FPG)

pressure side (PS), i.e. increase in the higher frequencies and decrease in the lower ones. The results follow the expected scaling of the wall-pressure spectrum as the thicker boundary layers on the suction side show higher amplitudes at larger scales (lower frequencies) while the thinner ones on the pressure side show higher amplitudes at smaller scales (higher frequencies) [25].

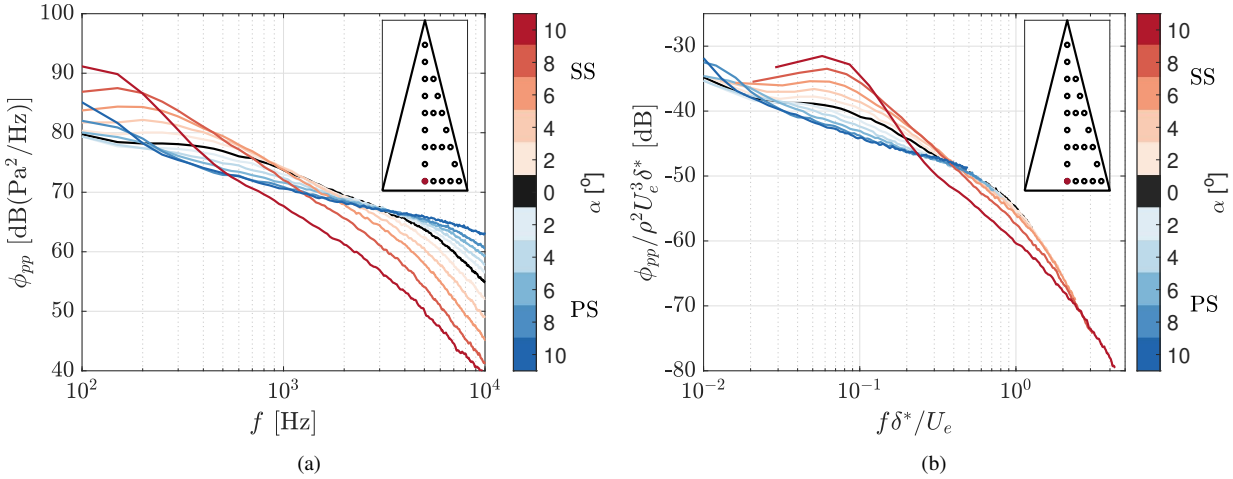

Fig. 6 Variation of the pressure spectrum at the root of the serration with frequency and Strouhal number for different angles of attack (Re = 2, 000, 000).

Besides the energy of the wall-pressure fluctuations, their average advection speed also influences the scattered noise. This parameter can be estimated with the time delay of maximum coherence between two streamwise spaced microphones, or, in the case of this work, with the derivative in the phase of the cross-spectrum of the same microphones with respect to the frequency, following the procedure described in Romano [26] (eq. 2). Fig. 7 depicts the variations in the mean convection velocity at the serration root with the angle of attack. Fig. 7(a) shows how the convection velocity increases at the pressure side and reduces at the suction side. The favourable pressure gradient in the pressure side is responsible for a boundary layer velocity profile with higher momentum flow closer to the wall. As a consequence, the surrounding velocity fluctuations that affect the wall pressure are advected at a higher speed, thus resulting in a higher convection velocity of the wall-pressure fluctuations. At the suction side, the same velocity fluctuations closer to the wall are subjected to a smaller mean velocity and, consequently, the captured convection velocity is reduced.

$$U_c = 2\pi\Delta x \frac{d\psi}{df}^{-1}. \tag{1}$$

The variation of the convective velocity with the boundary layer profile can be well described with its dependency on the boundary layer shape factor (H) in Fig. 7(b), similarly to the work of [27]. Data is shown in all three Reynolds numbers tested ($Re = 1,000,000$, $2,000,000$, and $3,000,000$) to demonstrate the consistency of the trends. As mentioned before, it can be seen that lower convection velocities are usually associated with higher boundary-layer shape factors (lower speed flows near the wall) and higher convection velocities with lower shape-factors (higher speed flows near the wall). This relationship can be expressed according to eq. 2. An experimental exponential fit is proposed combining the obtained convective velocities and boundary layer shape factors at the three Reynolds numbers tested. The proposed fit yields a representation of the convective speed for this experiment at the full range of boundary layer shape factors.

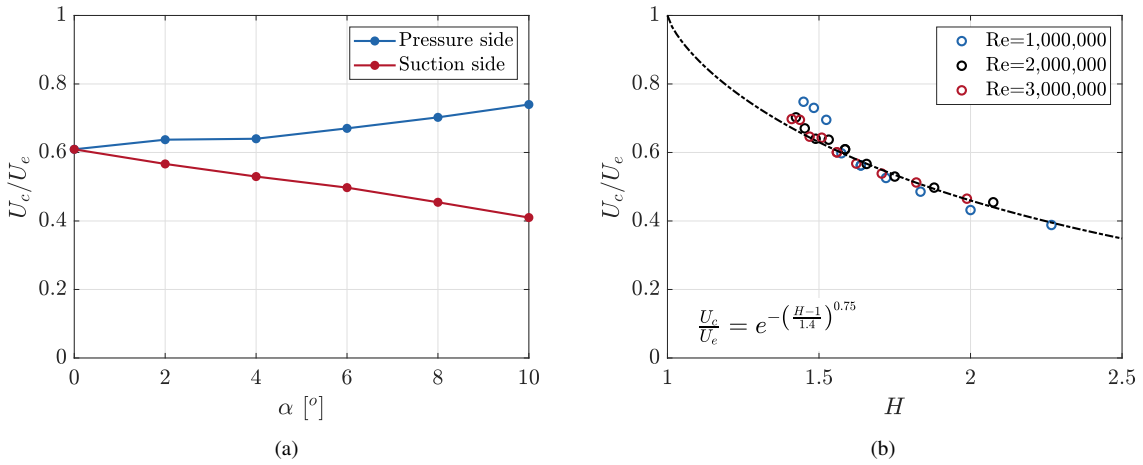

Fig. 7 Measured convective velocity at different angles of attack at Re = 2, 000, 000 (a) and fitting of the convective velocity with the boundary layer shape factor, H (b).

$$\frac{U_c}{U_e} = e^{-\left(\frac{H-1}{1.5}\right)^{3/4}}. \tag{2}$$

From the wall-pressure spectrum and the convection velocity one can already describe the wall-pressure fluctuations as a wavenumber frequency spectrum [28], following the requirements for analytical noise predictions [6–8]. Nevertheless, the correlation length is another fundamental quantity that impact trailing-edge noise [6]. It gives a measure of the average size of the wall-pressure structures in the boundary layer. This parameter determines the particular extension of the trailing edge that scatters noise coherently [29]. The analytical estimations of serration require the assumption of $l_x > 2h$ and, therefore, predictions obtained for smaller correlation lengths (higher frequencies) are less accurate.

The correlation length is defined by the integral of the coherence function γ in frequency domain along the span or streamwise direction [29] (eq. 3). In this work, this integral is computed after the fitting of the coherence values with an exponential function, following the assumption provided in Corcos [30]. This procedure improves the accuracy of the extracted quantities as it is more robust to noise and avoids truncation errors. The values of l_x, and l_z are commonly predicted to be directly proportional to the convection velocity and inversely proportional to the frequency ($l = U_c/k\omega$) [30], where k is estimated in 0.15 and 0.7 for the stream (l_x) and spanwise (l_z) correlation length respectively [31].

$$\begin{cases} l_x(\omega) = \int_0^\infty \gamma(\omega, \Delta z)\, dx, \\ l_z(\omega) = \int_0^\infty \gamma(\omega, \Delta z)\, dz. \end{cases} \tag{3}$$

Fig. 8 shows the measured stream and spanwise correlation lengths at the serration root for different angles of attack. At the Reynolds numbers investigated, the predictions of Corcos [30] are only valid at high frequencies (as observed in

Figs. 8(c) and 8(c) using the k values proposed by Hu & Herr [31]). A local maximum is captured for both correlation lengths, following the Efimtsov curve shape used in the work of Palumbo [32]. Nevertheless, the value and frequency of maximum correlation length seem to vary with the angle of attack. Besides, this maximum correlation length varies differently for the spanwise and streamwise correlation lengths, indicating that the two are not dependent on the same parameters. For the streamwise correlation length (l_x), all angles of attack tested seem to follow the trend predicted by Hu & Herr [31]. The local maximum is higher at the suction side and smaller at the pressure side. However, scaling the correlation length with the boundary layer displacement thickness show a nice collapse of the curves. The local maximum on the pressure side happens at a lower non-dimensional frequency and it corresponds to a higher ratio l_x/δ^*.

The spanwise correlation length follows a similar trend, i.e. lower maximum correlation lengths at the pressure side and higher ones at the suction side. Nevertheless, the non-dimensional plot reveals some important differences. At first, the trend proposed by Hu & Herr [31] is only valid for the $\alpha = 0°$. The suction side presents higher relative correlation lengths (l_z/δ^*) while the same value decreases at the pressure side with the angle of attack. Contrarily to the streamwise correlation length, the local maximum is constrained to values around $l_z/\delta^* = 3$ for all conditions tested.

In the streamwise direction, the Corcos equation using the empirical parameter $k = 0.15$ [31] yields good predictions for both favourable and adverse pressure gradient conditions. The maximum correlation length, however, seems to be relatively higher (l_x/δ^*) at favourable pressure gradient conditions.

In the spanwise direction (l_z), the high frequency decrease depends on the pressure gradient condition and the proposed $k = 0.7$ [31] is only valid for $\alpha = 0°$. The local maximum, however, is restricted to a non-dimensional value around $l_z/\delta^* = 3$.

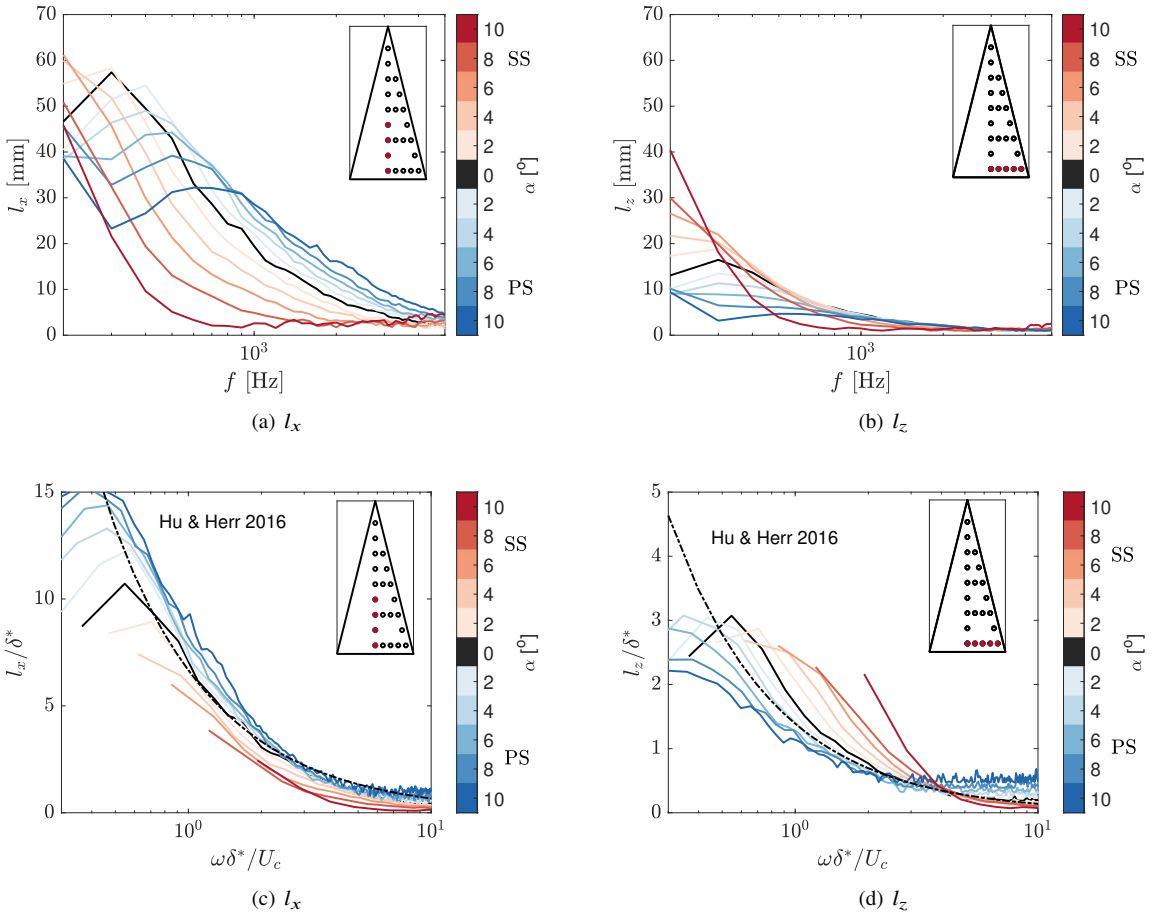

Fig. 8 Variation of the stream (a and c) and spanwise (b and d) correlation length at the root of the serration with frequency and Strouhal number for different angles of attack (Re = 2, 000, 000).

C. Distribution of the wall-pressure fluctuations over the serration without aerodynamic loading

Following the discussed properties of the incoming wall-pressure fluctuations, this section focuses on the description of the variations of the wall-pressure spectrum along the serration surface. These variations can be directly related to the discrepancies between measured and predicted far-field noise reduction since the former considers that the wall pressure is exactly the same over the entire serration surface. This section attempts to assess the captured modifications in the wall pressure observed when the serrations are not aerodynamically loaded, i.e. without any effect caused by the vortex pairs formed around the serration edges [10].

Fig. 9 shows the spectra captured at the sensors along the centre of the serrations. The figure demonstrates the variations of the wall pressure along the serration. At the root, the amplitude is higher at low frequencies and lower for higher frequencies. As one progresses from the root towards the tip the low frequency ($f < 2.0$ kHz) levels are reduced while the high-frequency ones increase. [13, 14] have reported a decrease in the wall-pressure root mean square from the root to the tip. This is also in agreement with the present observations as the higher overall amplitude in the low-frequency content contributes strongly to the root mean square values and, therefore, the decrease from the root to the tip of the serration dominates the analysis. Nevertheless, the high-frequency energy is also noted in the same references. The increase in high frequencies is related to the cut-off in the noise reduction obtained from trailing-edge serrations. Avallone et al. [13] have suggested that the noise is predominantly generated at the root of the serration in low frequencies and at the tip in high frequencies. This assumption follows the different locations of higher wall-pressure fluctuations at low frequencies (serration root) and at high frequencies (tip).

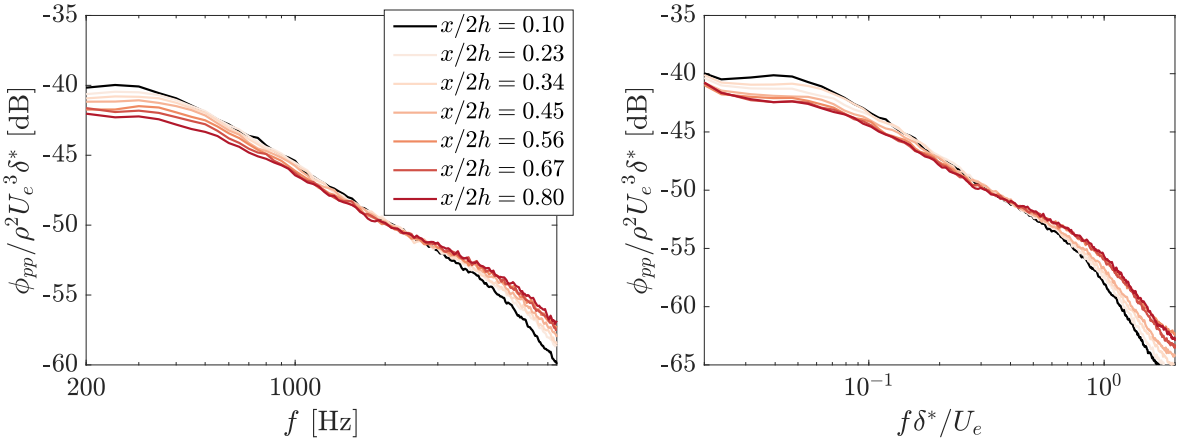

Fig. 9 Variation of the pressure spectrum along the serration centre with frequency (a) and Strouhal number (b) for $\alpha = 0°$ and $Re = 2,000,000$.

The variations of the wall pressure can be better observed from the interpolated distribution over the serration surface for different frequencies in Fig. 10. In the images, the sensor at the centre root is taken as the reference. Shades of blue indicate a reduction while shades of red indicate an increase of the wall-pressure fluctuations with respect to the incoming ones.

The images show the modifications discussed previously. At lower frequencies, the overall spectrum reduces from the centre root to the tip of the serration. This reduction is more intense and spread over the serration surface at lower frequencies (Figs. 10(a), 10(b)) and becomes milder and restricted to the serration edges at higher frequencies (Fig. 10(c)). At even higher frequencies (Figs. 10(e), 10(f)) a different trend is observed. The pressure fluctuations increase from root to tip. This latter trend is only dependent on the streamwise position and no significant variations are observed along the spanwise direction.

D. Effect of the angle of attack on the wall-pressure fluctuations over the serration surface

Having analyzed the distribution of the wall-pressure fluctuations without the presence of aerodynamic loading, this section focuses on the alterations of these wall-pressure fluctuations caused by the aerodynamic loading and the vortex pairs generated on the serration edges.

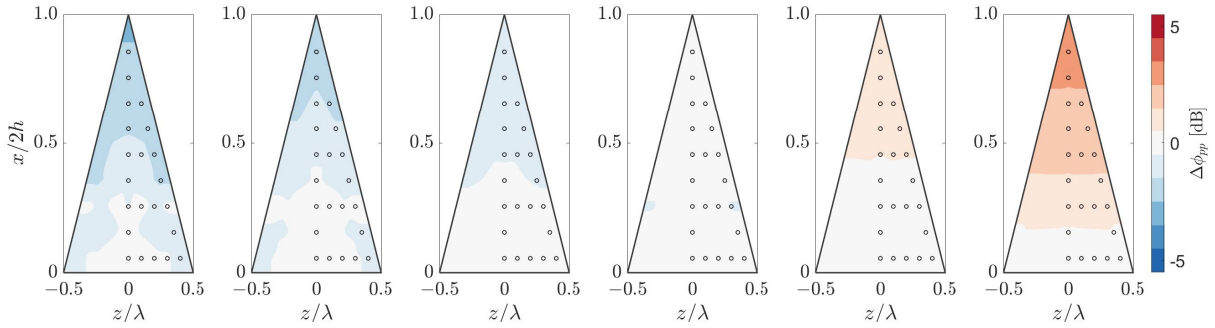

(a) f = 250 Hz (b) f = 500 Hz (c) f = 1000 Hz (d) f = 2000 Hz (e) f = 4000 Hz (f) f = 8000 Hz

Fig. 10 Wall-pressure fluctuations over the serration surface at $\alpha = 0°$ and $Re = 2 \times 10^6$. Reference is set to the sensor at the centre root of the serration.

Fig. 11 shows the progressing modification of the wall-pressure fluctuation distribution with the angle of attack at f = 500 Hz. Fig. 11 (a) to (f) show the data obtained at suction side while Fig. 11 (g) to (l) show the one obtained at the pressure side. From the graphs it is clear that the observed tendency at $\alpha = 0°$ is sustained for small angles (up to $\alpha = 4°$ at the suction side and $\alpha = 6°$ at the pressure side). At such conditions, aerodynamic loading does not seem to affect the wall-pressure spectrum and the surface distribution follows the trend described in Section IV.C at low frequencies. For higher angles, a visible increase of the wall-pressure fluctuations along the serration edges is captured. The increase is at first restricted to the tip of the serration for mild angles, e.g. $\alpha = 6°$, but it spreads towards the serration root for higher angles, e.g. $\alpha = 10°$. The effect is observed for angles of attack higher than 6° along the suction side and only at 10° at the pressure side. This difference is demonstrated later in the work and relates to the frequency dependency of these pressure fluctuations induced by the aerodynamic loading. For the selected frequency (f = 500 Hz), the fluctuations at the suction side are stronger than the ones at the pressure side.

The captured increase in the wall-pressure fluctuations due to the aerodynamic loading is often related to the formation of a vortex pair at the serration edge and to the increase in noise from serrated trailing edges at an angle [10, 16].

This increase in the wall-pressure levels along the serration edge is also frequency dependent. Fig. 12 depicts how the measured spectrum modifies along the serration edge at $\alpha = 10°$ for frequencies from 250 to 8000 Hz. Again, Figs 12(a) to (f) show the wall-pressure fluctuations at the suction side and Figs 12(g) to (l) at the pressure side.

The distribution of the wall-pressure levels analyzed in different frequencies shows that the effects of the aerodynamic loading are frequency dependent and also that it varies from the suction to the pressure side. The effects are generally concentrated on a narrow band of frequencies. On the suction side, stronger modifications are observed around f = 250 Hz. On the pressure side, the same is only observed around f = 2000 Hz.

These discrepancies are attributed to the different scales and velocities of the convecting pressure fluctuations that interact with the vortex pairs. On both sides, the non-dimensional Strouhal number based on the boundary layer displacement thickness $f\delta^*/U_c$ in which the effect is stronger yields similar values (0.20 and 0.18 at the pressure and suction side respectively). This similarity between the two values indicates that the phenomenon depends also on the properties of the incoming turbulent boundary layer. This means that the accelerations of the mean flow influence the larger and slower structures from the suction side and the smaller and faster ones from the pressure side. This influence gets stronger with the aerodynamic loading of the serration, indicating that the interaction between the vortex pairs and the incoming turbulent structures is responsible for the increased pressure fluctuations on the serration edges.

This effect can increase the pressure fluctuations by more than 5 dB on the edge of the serrations. Such values are in the order of the quoted trailing-edge noise in many applications [9] and indicate how the vortex pairs can influence the scattered noise.

V. Conclusions

Measurements of the wall-pressure fluctuations on the surface of a serrated trailing edge of the benchmark NACA 63_3-018 airfoil are carried out. Results show the properties of the incoming wall-pressure fluctuations at the serration root and their modifications along the serration surface under different flow conditions.

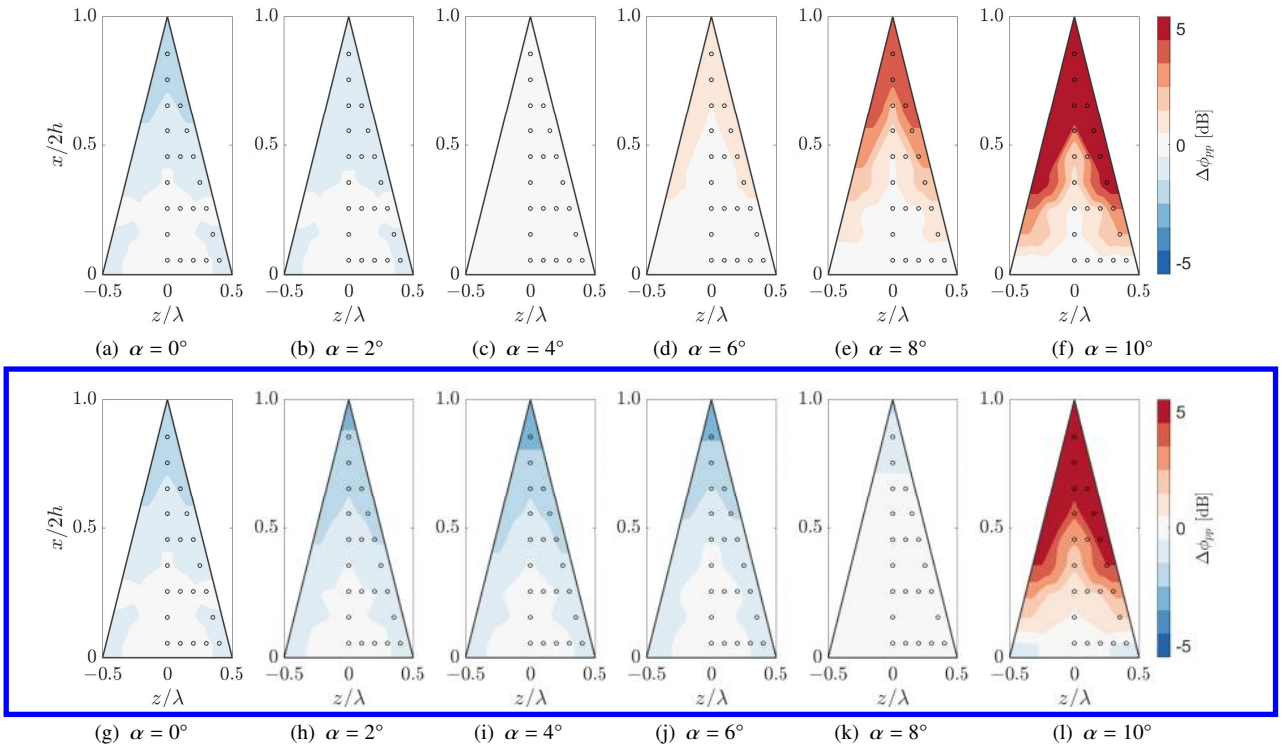

Fig. 11 Wall-pressure fluctuations over the serration surface for $f = 500$ Hz at different angles of attack and $Re = 2 \times 10^6$. Reference is set to the sensor at the centre root of the serration. Figures (a) to (f) shows the measured wall-pressure levels at the suction side and figures (g) to (l) at the pressure side.

Without aerodynamic loading, the wall-pressure fluctuations are higher at the root of the serration and decrease progressively as one moves towards the tip of the serration. This pattern is more strongly observed in low frequencies and gets milder as the frequency increases. At very high frequencies this trend is reverted and pressure fluctuations are higher at the tip than at the root of the serrations. Results are in agreement with other observations [13, 14] and point to a stronger scattering at the serration root with respect to the one at the serration tip at lower frequencies and the inverse to happen at higher frequencies, i.e. conditions at the tip of the serration dominate the scattered noise.

The aerodynamic loading causes an increase in the wall-pressure fluctuations at the outer rim of the serration. This increase is stronger around $f\delta^*/U_e \approx 0.2$ and is related to the accelerations of the flow imposed by the trailing vortices formed at the serration interacting with the incoming turbulent boundary layer fluctuations. Again, these modifications can be related to decreasing efficiency of the serration devices observed in other references [33].

Overall, it is shown that meaningful variations occur in the wall-pressure fluctuations along the serration surface. Deviations from the measurements at the root are as large as 5 dB, similar to the quoted noise reductions achieved with serrated devices. Consequently, accurate noise predictions from serrated trailing edge noise are dependent on a proper description of those deviations, and predictions based solely on the incoming wall-pressure fluctuations from the turbulent boundary layer are prone to major deviations from the measurements.

The results presented here contribute to the future BANC activities by providing experimental data of the wall-pressure fluctuations over the serration surface. The data could contribute to further attempts of modelling or simulating the present benchmark configuration.

Acknowledgments

This study is supported by the SMARTANSWER project (Smart Mitigation of flow-induced Acoustic Radiation and Transmission for reduced Aircraft, surface traNSport, Workplaces and wind enERgy noise) which has received funding from the European Union's Horizon 2020 research and innovation program under the Marie Skłodowska-Curie grant agreement No. 722401. More information can be found on https://www.h2020-smartanswer.eu. The authors would like

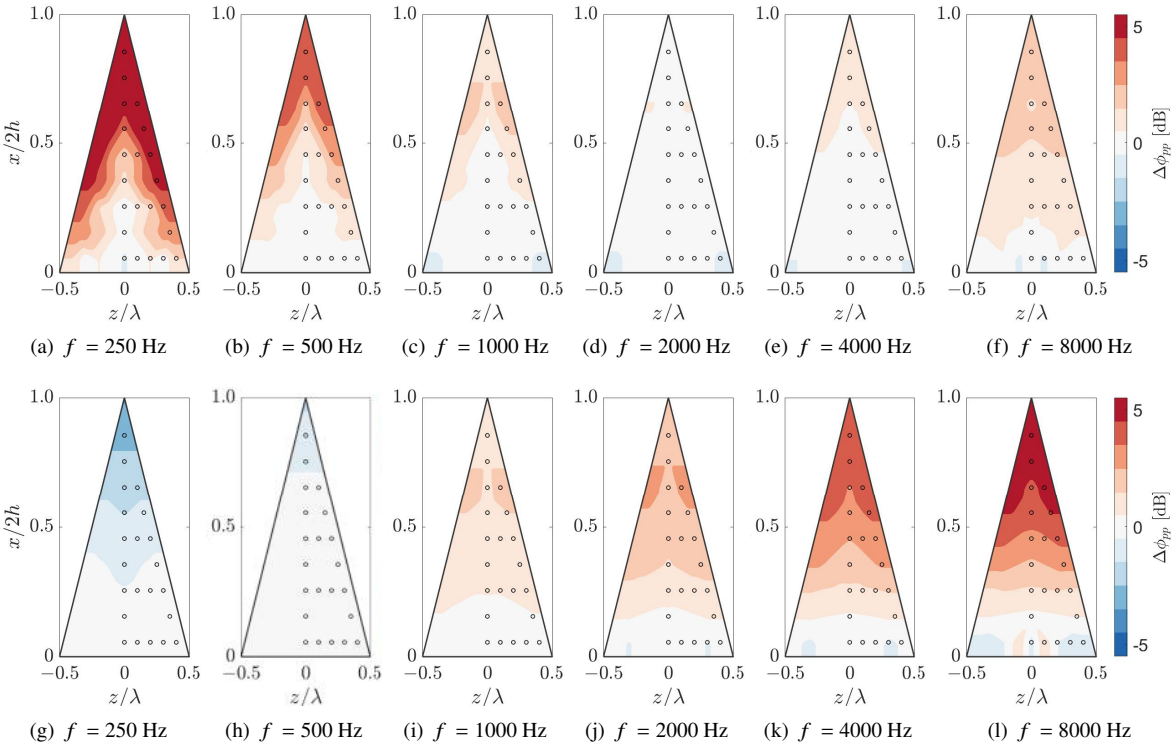

Fig. 12 Wall-pressure fluctuations over the serration surface for $\alpha = 10°$ and $Re = 2 \times 10^6$. Reference is set to the sensor at the centre root of the serration.

to acknowledge Andreas Fischer for proving the wind tunnel model and assisting on the benchmarking activities, Salil Luesutthiviboon for the help throughout the experimental campaign, Stefan Oerlemans, Oriol Ferret Gasch, and Pranav Manjunath for assisting in the preparations and definitions of the experimental campaign.

References

[1] Council of Canadian Academies, *Understanding the evidence: Wind Turbine noise The Expert Panel on Wind Turbine Noise and Human Health*, March, 2015. URL `https://cca-reports.ca/reports/understanding-the-evidence-wind-turbine-noise/`.

[2] Oerlemans, S., *Detection of aeroacoustic sound sources on aircraft and wind turbines*, 2009.

[3] Asheim, M. J., Ferret Gasch, O., and Oerlemans, S., "Rotor blade with a serrated trailing edge," , 2017.

[4] Howe, M., "Aerodynamic noise of a serrated trailing edge," *Journal of Fluids and Structures*, Vol. 5, No. 1, 1991, pp. 33–45. https://doi.org/10.1016/0889-9746(91)80010-B, URL https://linkinghub.elsevier.com/retrieve/pii/088997469180010B.

[5] Howe, M. S., "Noise produced by a sawtooth trailing edge," *The Journal of the Acoustical Society of America*, Vol. 90, No. 1, 1991, pp. 482–487. https://doi.org/10.1121/1.401273.

[6] Lyu, B., Azarpeyvand, M., and Sinayoko, S., "Prediction of noise from serrated trailing edges," *Journal of Fluid Mechanics*, Vol. 793, 2016, pp. 556–588. https://doi.org/10.1017/jfm.2016.132.

[7] Ayton, L. J., "Analytic solution for aerodynamic noise generated by plates with spanwise-varying trailing edges," *Journal of Fluid Mechanics*, Vol. 849, No. August, 2018, pp. 448–466. https://doi.org/10.1017/jfm.2018.431.

[8] Lyu, B., and Ayton, L. J., "Serrated leading-edge and trailing-edge noise prediction models for realistic wavenumber frequency spectra," , No. May, 2019. https://doi.org/10.2514/6.2019-2674.

[9] Gruber, M., Joseph, P., and Chong, T., "On the mechanisms of serrated airfoil trailing edge noise reduction," *17th AIAA/CEAS Aeroacoustics Conference (32nd AIAA Aeroacoustics Conference)*, , No. June, 2011, pp. 5–8. https://doi.org/10.2514/6.2011-2781, URL http://arc.aiaa.org/doi/10.2514/6.2011-2781.

[10] Arce León, C., Ragni, D., Pröbsting, S., Scarano, F., and Madsen, J., "Flow topology and acoustic emissions of trailing edge serrations at incidence," *Experiments in Fluids*, Vol. 57, No. 5, 2016. https://doi.org/10.1007/s00348-016-2181-1.

[11] Ragni, D., Avallone, F., van der Velden, W. C. P., and Casalino, D., "Measurements of near-wall pressure fluctuations for trailing-edge serrations and slits," *Experiments in Fluids*, Vol. 60, No. 1, 2019, p. 6. https://doi.org/10.1007/s00348-018-2654-5, URL http://link.springer.com/10.1007/s00348-018-2654-5.

[12] Jones, L. E., and Sandberg, R. D., "Acoustic and hydrodynamic analysis of the flow around an aerofoil with trailing-edge serrations," *Journal of Fluid Mechanics*, Vol. 706, 2012, pp. 295–322. https://doi.org/10.1017/jfm.2012.254.

[13] Avallone, F., van der Velden, W. C., and Ragni, D., "Benefits of curved serrations on broadband trailing-edge noise reduction," *Journal of Sound and Vibration*, Vol. 400, No. April, 2017, pp. 167–177. https://doi.org/10.1016/j.jsv.2017.04.007, URL http://dx.doi.org/10.1016/j.jsv.2017.04.007.

[14] Avallone, F., van der Velden, W. C., Ragni, D., and Casalino, D., "Noise reduction mechanisms of sawtooth and combed-sawtooth trailing-edge serrations," *Journal of Fluid Mechanics*, Vol. 848, No. June, 2018, pp. 560–591. https://doi.org/10.1017/jfm.2018.377.

[15] Taylor, G. I., "The Spectrum of Turbulence," *Proceedings of the Royal Society of London. Series A - Mathematical and Physical Sciences*, Vol. 164, No. 919, 1938, pp. 476–490. https://doi.org/10.1098/rspa.1938.0032, URL http://www.royalsocietypublishing.org/doi/10.1098/rspa.1938.0032.

[16] Arce León, C., Merino-Martínez, R., Ragni, D., Avallone, F., Scarano, F., Pröbsting, S., Snellen, M., Simons, D. G., and Madsen, J., "Effect of trailing edge serration-flow misalignment on airfoil noise emissions," *Journal of Sound and Vibration*, Vol. 405, 2017, pp. 19–33. https://doi.org/10.1016/j.jsv.2017.05.035, URL http://dx.doi.org/10.1016/j.jsv.2017.05.035.

[17] Avallone, F., Pröbsting, S., and Ragni, D., "Three-dimensional flow field over a trailing-edge serration and implications on broadband noise," *Physics of Fluids*, Vol. 28, No. 11, 2016. https://doi.org/10.1063/1.4966633.

[18] Lima Pereira, L. T., Ragni, D., Avallone, F., and Scarano, F., "Pressure fluctuations from large-scale PIV over a serrated trailing edge," *Experiments in Fluids*, Vol. 61, No. 3, 2020, pp. 1–17. https://doi.org/10.1007/s00348-020-2888-x, URL https://doi.org/10.1007/s00348-020-2888-x.

[19] Sanders, M. P., De Santana, L. D., Azarpeyvand, M., and Venner, C. H., "Unsteady surface pressure measurements on trailing edge serrations based on digital MEMS microphones," *2018 AIAA/CEAS Aeroacoustics Conference*, 2018, pp. 1–12. https://doi.org/10.2514/6.2018-3290.

[20] Merino-Martínez, R., Rubio Carpio, A., Lima Pereira, L. T., van Herk, S., Avallone, F., Ragni, D., and Kotsonis, M., "Aeroacoustic design and characterization of the 3D-printed, open-jet, anechoic wind tunnel of Delft University of Technology," *Applied Acoustics*, Vol. 170, 2020. https://doi.org/10.1016/j.apacoust.2020.107504.

[21] Raffel, M., Willert, C. E., Scarano, F., Kähler, C. J., Wereley, S. T., and Kompenhans, J., *Particle Image Velocimetry*, 2018. https://doi.org/10.1007/978-3-319-68852-7, URL http://link.springer.com/10.1007/978-3-319-68852-7.

[22] Clauser, F. H., "The Turbulent Boundary Layer," *Advances in Applied Mechanics*, Vol. 4, No. C, 1956, pp. 1–51. https://doi.org/10.1016/S0065-2156(08)70370-3.

[23] Coles, D., "The law of the wake in the turbulent boundary layer," *Journal of Fluid Mechanics*, Vol. 1, No. 2, 1956, pp. 191–226. https://doi.org/10.1017/S0022112056000135.

[24] Rozenberg, Y., Robert, G., and Moreau, S., "Wall-pressure spectral model including the adverse pressure gradient effects," *AIAA Journal*, Vol. 50, No. 10, 2012, pp. 2168–2179. https://doi.org/10.2514/1.J051500.

[25] Hwang, Y. F., Bonness, W. K., and Hambric, S. A., "Comparison of semi-empirical models for turbulent boundary layer wall pressure spectra," *Journal of Sound and Vibration*, Vol. 319, No. 1-2, 2009, pp. 199–217. https://doi.org/10.1016/j.jsv.2008.06.002.

[26] Romano, G. P., "Analysis of two-point velocity measurements in near-wall flows," *Experiments in Fluids*, Vol. 20, No. 2, 1995, pp. 68–83. https://doi.org/10.1007/BF00189296.

[27] Ryan Catlett, M., Anderson, J. M., Forest, J. B., and Stewart, D. O., "Empirical modeling of pressure spectra in adverse pressure gradient turbulent boundary layers," *AIAA Journal*, Vol. 54, No. 2, 2016, pp. 569–587. https://doi.org/10.2514/1.J054375.

[28] Roger, M., and Moreau, S., "Back-scattering correction and further extensions of Amiet's trailing-edge noise model. Part 1: Theory," *Journal of Sound and Vibration*, Vol. 286, No. 3, 2005, pp. 477–506. https://doi.org/10.1016/j.jsv.2004.10.054.

[29] Amiet, R. K., "Noise due to turbulent flow past a trailing edge," *Journal of Sound and Vibration*, Vol. 47, No. 3, 1976, pp. 387–393. https://doi.org/10.1016/0022-460X(76)90948-2.

[30] Corcos, G. M., "Resolution of Pressure in Turbulence," *The Journal of the Acoustical Society of America*, Vol. 35, No. 2, 1963, pp. 192–199. https://doi.org/10.1121/1.1918431.

[31] Hu, N., and Herr, M., "Characteristics of wall pressure fluctuations for a flat plate turbulent boundary layer with pressure gradients," *22nd AIAA/CEAS Aeroacoustics Conference, 2016*, 2016, pp. 1–18. https://doi.org/10.2514/6.2016-2749.

[32] Palumbo, D., "Determining correlation and coherence lengths in turbulent boundary layer flight data," *Journal of Sound and Vibration*, Vol. 331, No. 16, 2012, pp. 3721–3737. https://doi.org/10.1016/j.jsv.2012.03.015, URL http://dx.doi.org/10.1016/j.jsv.2012.03.015.

[33] Arce León, C., Ragni, D., Pröbsting, S., Scarano, F., and Madsen, J., "Flow topology and acoustic emissions of trailing edge serrations at incidence," *Experiments in Fluids*, Vol. 57, No. 5, 2016. https://doi.org/10.1007/s00348-016-2181-1.